Climatology in shallow caves with negligible ventilation: heat and mass transfer

Béatrice Guerrier[a,*], Frédéric Doumenc[a,b], Aymeric Roux[a], Sophie Mergui[a,b], Pierre-Yves Jeannin[c]

[a] *Laboratoire FAST, Univ. Paris-Sud, CNRS, Université Paris-Saclay, F-91405, Orsay, France*

[b] *Sorbonne Université, UFR 919, 4 place Jussieu, F-75252, Paris Cedex05, France*

[c] *Swiss Institute for Speleology and Karstology (SISKA), CH-2301, La Chaux-de-Fonds, Switzerland*

Abstract

The present numerical study investigates the effect of a cavity located at shallow depth below ground surface. The temperature field in the rock matrix surrounding the cave is significantly deformed compared to the case without cavity. Fluxes at cave wall, related to radiation, air-convection and evaporation/condensation (in case of a humid cave), all contribute to a significant homogenization of wall temperatures. In case of high humidity, simulations of evaporation/condensation periods show that some parts of the wall may be durably (several months) subjected to significant condensation (or evaporation). Real meteorological data, i.e. 77 years of external temperature data of the Gourdon station in France, have been used as input of the model. Results of simulations have been compared to experimental temperature of Lascaux cave, with good agreement considering some simplifying hypotheses assumed for this modeling. The asset of such a model is the low computing time required to simulate several years, and thus its ability to follow long time evolution. Results significantly improve our understanding of conditions taking place in a shallow cavity, what will help improving the management of caves, especially those with very fragile decorations such as Paleolithic paintings. The model may help to identify areas which are the most exposed to weathering and to test the effect of past and potential changes in nearby conditions. It may also be useful for managing shallow underground constructions (e.g. a mine or even a cellar).

Keywords: cave - karstic massif - temperature - humidity - heat transfer - condensation -

*Corresponding author, guerrier@fast.u-psud.fr, FAST, Bât. Pascal (n^{o}530), Campus Universitaire, 91405 Orsay, France

1. Introduction

Caves represent fragile ecosystems where biogeochemical processes largely depend on cave temperature and humidity. Caves also host unique environmental records and paleolithic wall-paintings whose conservation closely depends on cave climate as well. Yet little is known about the relative importance of individual mechanisms transferring heat from the surface to the cave environment. Achieving a good understanding of the thermal response of caves to climate change or to perturbations is central to protect cave painting [1, 2, 3, 4] and organisms living in karst [5, 6, 7], as well as to interpret paeloenvironmental indicators recorded in speleothems such as dissolution/precipitation rates [8, 9], and geochemical partitioning [10].

Temperature and humidity variations are usually very little in caves [5, 11, 12]. This very stable environment strongly slows down weathering processes. This explains why wall paintings could be preserved through many thousands of years (e.g. 18 000 years in the case of Lascaux cave). The absence of rain, frost, sun and temperature change strongly reduces the number and the effect of processes able to damage the wall surface [13, 14, 15].

Temperature on Earth surface is known to change with daily, seasonal, decadal and longer cycles. The amplitude of these variations decreases with depth depending on their time scale [16]. Depending on the rock diffusivity, daily variations are smoothed away to 99% at about one meter depth, yearly cycles at about 15 meters, and longer variations propagate deeper (e.g. [17, 18]). Data from boreholes from all over the world confirm that in most cases temperature smoothing with depth behaves according to heat conduction through a more or less homogeneous medium (bedrock). The overall temperature gradient depends on the intensity of the heat flux and on the value of the rock heat conductivity [19]. In the near surface ($\sim$ 10 m) the rock temperature is mainly controlled by the outside temperature, which varies considerably along the year. Therefore, in this zone the temperature gradient varies with the season and the depth. Close to the surface, its maximum value is a few degrees per meter and it changes sign between winter and summer. The zone with annual temperature variations larger than $\sim 5\%$ of the outside temperature variation is often called "heterothermic zone" [20]. The deeper part of the massif, with a stable temperature all along the year, is called "homothermic zone" by the same author.

The present paper focusses on heat transfer in a karst massif including caves or cavities located

within the heterothermic zone, also sometimes labelled as "shallow caves". As an illustration, we use a geometry which partially mimics the entrance part (Hall of Bulls) of the Lascaux cave in France. This cave is almost not ventilated and belongs to "confined cave" according to the definition given by Bourges et al. [12]. De Freitas and co-authors [21, 22, 23] also studied climate of a shallow cave, but conversely to Lascaux, Glowworm Cave is strongly ventilated.

Shallow caves, but also mines or tunnels are voids cutting across the rock medium. With a size of several meters they create a disruption in the conductive medium (bedrock). Therefore, temperature along their respective walls is not uniform inducing heat exchanges within the cavity. Air humidity in underground voids is usually close to vapor saturation. This is at least the case in caves with a reduced air exchange with the outside atmosphere, such as Lascaux cave [24]. In this situation any change in temperature may produce condensation or evaporation at the cave wall. This specific environment (wall with condensation water) seems to enhance the development of bacterial or fungic mats [25], which in turn can produce weathering of the wall surface.

The aim of the present study is to assess the shape and evolution of the temperature field produced by a void within the heterothermic zone, and to assess heat exchanges inside the cavity in order to evaluate the position, seasonality and quantity of condensation/evaporation taking place at cave walls. The study example is based on data from Lascaux cave but provides indications about processes taking place in any cave, mines or tunnels located at shallow depth (less than about 15 meters below ground). Conditions in this environment are important for the preservation of Paleolithic painted caves, but it provides also an interesting base for understanding habitats in this part of the critical zone [26], as well as for interpreting paleoclimatic records from speleothemes.

Since the purpose of this study is to highlight the general trends that characterize the thermal behavior of shallow caves, the conceptual model used in the following keeps only the main characteristics of the configuration of such caves and uses some simplifying assumptions. Concerning the rock matrix surrounding the cavity, heat is assumed to be transferred only by conduction through a homogeneous rock. Advection due to air or water flows is assumed to be negligible. In the case studied here the cave is assumed to be sufficiently far from other similar caves.

Temperature at ground surface is given by air temperature and is assumed uniform, i.e. we do not take into account spatial variations due for instance to different expositions to solar insulation.

Concerning the overall heat flux from the bottom of the karst aquifer, measurements in many karst massifs showed that the flux of water at the bottom of the karst aquifer is usually high enough

to drain away most of the geothermal heat. Observed gradients typically range between 0.23 and 0.6°C per 100 meters [27, 28, 29]. This gradient (and corresponding flux) is low compared to the usual geothermal gradient of ~ 3°C/100m. Thus most of the simulations are performed under the assumption of zero flux at the bottom of the karst aquifer. Some simulations using a geothermal gradient of ~ 3°C/100 m are also performed in order to estimate the influence of such a gradient on the thermal behavior of the cavity.

Finally the cave is assumed to be "confined", i.e. without any significant exchange of air with the outside atmosphere. In Lascaux cave, the presence of two succeeding air-locks at the cave entrance, as well as measurements of cave and outside atmosphere (temperature, pressure) made by Schoeller [30], Vouvé et al. [31], and Malaurent et al. [24] show that some exchange still takes place, but are rather low.

Temperature variations in Lascaux cave are small (less than 1°C) and differences between air and rock temperature even smaller (~ 0.1°C). Air humidity measured in the cave always ranges between 98 and 100% [31]. In these conditions all fluxes are small and smooth, meaning that small temperature differences may shift conditions from evaporation to condensation or the opposite.

Inside the cavity, processes considered in the physical model are convection of air within the cave volume, heat radiation between facing walls and evapo-condensation at cave walls. In order to limit the complexity of the model and to get "reasonable" computing time for simulations over long periods (several decades), the model is 2D and the description of convection is simplified.

The paper is organised as follows: the geometry, physical model, thermophysical properties and numerical method used for the simulations are described first. Then the thermal response of the cavity to a periodic yearly variation of the external temperature is considered. The perturbation induced by the cavity in the massif, the relative weight of the different heat transfer modes in the cavity and the evaporation/condensation phases are deduced from the analysis of this periodic regime. Finally real meteorologic data (77 years) of the external temperature are used as input of the model and simulation results are compared to experimental data collected in Lascaux cave. Some suggestions to go further in the representation of such shallow cavities are drawn in the conclusion.

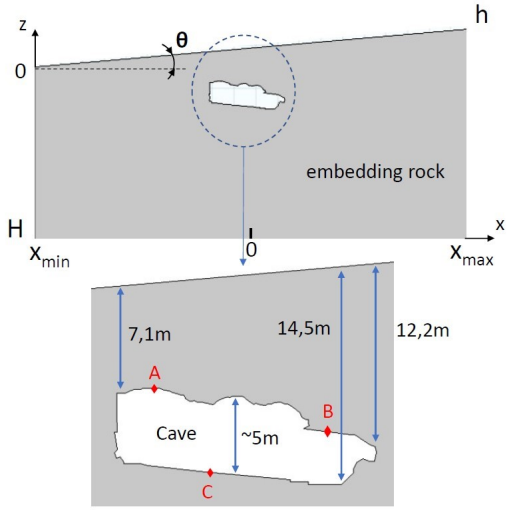

Figure 1: Top: computational model $\mathcal{D} = \mathcal{C} \cup \mathcal{M}$, including the cavity $\mathcal{C}$ and the surrounding karst massif $\mathcal{M}$. Bottom: zoom on the cavity, with the position of the three fictive sensors A, B and C.

2. Modeling

2.1. Domain geometry

We consider a cave embedded in a karst massif. The geometry, inclination and location of the cavity in the massif partially mimics the entrance passage of the Lascaux cave in France. Figure 1 shows the computational domain $\mathcal{D}$ that includes the karst massif $\mathcal{M}$ and the cave $\mathcal{C}$. For the sake of simplicity, the geometry is 2D. The cave is closed, i.e. there is no mass transfer between the cave and the surroundings.

The size of the computational domain $\mathcal{D}$ is $H = -40\,\mathrm{m}$, $h = 8.75\,\mathrm{m}$, $x_{min} = -51\,\mathrm{m}$, $x_{max} = 49\,\mathrm{m}$. The tilt of the upper surface, θ, is 5^o. The vertical distance d_v from the cave to the external ground surface is close to 7 m and 14.5 m for the highest and lowest points, respectively (cf. Figure 1, with $d_v = -z + (x - x_{min}) \tan\theta$). The height inside the cave is about 5 m in most of the cavity. The cross-section of the cavity is $74.6\,\mathrm{m}^2$ (i.e. volume per unit length in the transverse direction) and the perimeter is 44.3 m.

Three fictive "sensors" located in the upper or lower part of the ceiling and on the floor will be used in the following to analyze the results (cf. red symbols in Figure 1). Their coordinates $(x; z)$ are $(-8.19\,\mathrm{m}; -3.30\,\mathrm{m})$ for A sensor, $(3.40\,\mathrm{m}; -6.15\,\mathrm{m})$ for B sensor, and $(-3.92\,\mathrm{m}; -8.85\,\mathrm{m})$ for C sensor. The respective depths d_v are 7.05 m, 10.91 m and 12.97 m for A, B and C sensors.

2.2. Karst massif

Assuming that heat transfer is mainly conductive in the embedding rock with a constant diffusivity (homogeneous rock), the temperature at each point inside the domain $\mathcal{M}$ satisfies the heat equation

$$\frac{\partial T}{\partial t} = a_r \left(\frac{\partial^2 T}{\partial x^2} + \frac{\partial^2 T}{\partial z^2} \right) , \tag{1}$$

where $T(x, z, t)$ is the local temperature in $\mathcal{M}$, x and z are the horizontal and vertical coordinates, respectively, and a_r is the rock diffusivity ($\mathrm{m}^2.\mathrm{s}^{-1}$).

The external boundary conditions for the sub-domain $\mathcal{M}$ are the followings:

- Lateral boundary conditions: the computational domain $\mathcal{D}$ being much larger than the size of the cave, the perturbation resulting from the presence of the shallow cavity is negligible at the lateral boundaries of the domain and the flux is set to zero:

$$\left.\frac{\partial T}{\partial x}\right|_{x=x_{min}} = \left.\frac{\partial T}{\partial x}\right|_{x=x_{max}} = 0. \tag{2}$$

- Top boundary condition: at the external ground surface, the temperature is imposed (Dirichlet condition)

$$T(x, z, t) = T_{ex}(t) \quad \text{for} \quad x_{min} < x < x_{max} \quad \text{and} \quad z = (x - x_{min}) \tan\theta, \tag{3}$$

  where $T_{ex}(t)$ is the time varying outside temperature. We use in the following a periodic variation with a yearly period or real meteorological data.

- Bottom boundary condition: the choice of the bottom boundary condition is more challenging, as it requires a model of the karst massif at large scale. For instance, the presence of underground aquifer would imply a temperature condition. One can also use the estimation of the underground vertical temperature gradient in typical karst massif. This gradient is low (about 0.55 °C/100 m, compared to the usual 3 °C/100 m geothermal gradient, cf. for instance [29]). Since this study focuses on the cavity, we neglect the flux at the bottom of the domain ($z = H$). The influence of this assumption on the estimation of heat transfer in the shallow cavity is analyzed in the result section. Thus, except when explicitly mentioned, we

use

$$\left.\frac{\partial T}{\partial z}\right|_{z=H} = 0 \quad \text{for} \quad x_{min} < x < x_{max}. \tag{4}$$

The last boundary condition for the sub-domain $\mathcal{M}$ concerns the frontier with the cavity $\mathcal{C}$. The balance of thermal fluxes used to express the coupling between the embedding rock and the cavity is detailed in the next section.

2.3. Cavity

The cavity is filled with humid air in contact with the cavity wall. Air density decreases when temperature or water vapor concentration increase and several flow regimes may be observed depending on the spatial variation of air density in the cave. Air humidity being often close to saturation in closed caves, small temperature differences between wall and air are large enough to induce evaporation or condensation on part of the wall. If the cave floor is colder than the cave ceiling, the configuration is stable and no convection is expected. In the reverse configuration, density gradient in the air may induce convection.

In the convective regime, temperature and humidity gradients are mainly localized in thin layers close to the wall, the so-called boundary layers. The characterization of heat and mass transfer through these boundary layers would require to solve Navier Stokes equations, taking into account the variation of air density with temperature and humidity. Corresponding simulations are very time-consuming and thus not compatible with a study over long time scales. Hence we use a simplified description and assume that humid air in the cavity is described by a single temperature $T_a(t)$ and a single water vapor concentration $c_w(t)$. We also assume that (i) air properties do not depend on temperature and humidity, (ii) air is transparent for thermal radiation, (iii) evaporation or condensation takes place at the cavity wall only.

The time evolution of T_a results from the convective heat transfer with the cavity wall. With the assumption of a closed cavity, the energy balance reads

$$M_a c_a \frac{\mathrm{d}T_a}{\mathrm{d}t} = \iint_S \varphi_{conv} \, \mathrm{d}S \, , \tag{5}$$

where M_a is the total mass of air in the cavity, c_a is the air heat capacity at constant pressure ($\mathrm{J.kg^{-1}.K^{-1}}$), S is the surface of the cavity wall, and φ_{conv} ($\mathrm{W.m^{-2}}$) is the local convective heat

flux. It is given by the Newton law,

$$\varphi_{conv} = h_{th}(T - T_a), \tag{6}$$

where $T(x, z, t)$ is the local wall temperature. In the simplified model used in this study, the heat transfer coefficient h_{th} ($\mathrm{W.m^{-2}.K^{-1}}$) is assumed constant. The order of magnitude of h_{th} may be estimated by $h_{th} \sim \lambda_a/\delta_T$, with λ_a ($\mathrm{W.m^{-1}.K^{-1}}$) the air conductivity and δ_T the thermal boundary layer thickness (see Appendix A for more details).

The mass balance for water reads

$$V_{cave}\ \frac{\mathrm{d}c_w}{\mathrm{d}t} = \rho_w \iint_S v_{ev}\,\mathrm{d}S\ , \tag{7}$$

where V_{cave} is the volume of the cave (i.e. cavity section $\times$ the unit length in the tranverse direction), c_w is the water vapor concentration ($\mathrm{kg.m^{-3}}$), ρ_w is the liquid water density ($\mathrm{kg.m^{-3}}$) and v_{ev} ($\mathrm{m.s^{-1}}$) is the local evaporation rate (i.e. the volume of liquid water that evaporates by unit of time and surface, positive for evaporation).

Similarly to the thermal model, we use a description based on a constant mass transfer coefficient to express the local evaporation rate v_{ev},

$$v_{ev} = h_m\left(c_{sat} - c_w\right)/\rho_w, \tag{8}$$

where h_m ($\mathrm{m.s^{-1}}$) is the mass transfer coefficient and c_{sat} ($\mathrm{kg.m^{-3}}$) is the vapor concentration just above the liquid film on the wall. Evaporation fluxes being very weak, local thermodynamic equilibrium is assumed at the liquid/gas interface. In the air, the thicknesses of the thermal and solutal boundary layers are of the same order of magnitude. Thus the mass transfer coefficient may be estimated by $h_m\,(\mathrm{m.s^{-1}}) \sim \mathrm{D_w}/\delta_\mathrm{T}$, where D_w ($\mathrm{m^2.s^{-1}}$) is the diffusivity of vapor in air [32].

Two limiting cases are studied: we consider dry air (i.e. no evaporation or condensation, $v_{ev} = 0$) or we assume that there is always a liquid film on the wall. We assume that this water film is thin enough to neglect its conductive thermal resistance compared to the resistance induced by convection in the air, but thick enough to cover entirely the wall roughness at small scales and to be considered as a flat film. Thus we do not take into account the Kelvin effect, i.e. the decreasing of c_{sat} due to the presence of curved interfaces in micro-pores (see [33] for more details). With these

assumptions c_{sat} reads

$$c_{sat} = P_{sat}(T)\ M_w/(R\,T), \tag{9}$$

where R is the gas constant, M_w is the water molar mass and P_{sat} is the saturating vapor pressure at the local temperature of the wall T.

The wall boundary condition is provided by the energy balance [34]:

$$\varphi_{cond} = \varphi_{conv} + \varphi_{rad} + \varphi_w \tag{10}$$

where φ_{cond} ($\mathrm{W.m^{-2}}$) is the local conductive heat flux coming from the embedding rock, φ_{conv} is the local convective heat flux due to the exchange with the air of the cavity, φ_{rad} is the local net radiative heat flux and φ_w comes from evaporation or condensation latent heat. This equation ensures the coupling between the embedding rock $\mathcal{M}$ and the cave $\mathcal{C}$.

- The conductive flux is

$$\varphi_{cond} = \vec{n}.[-\lambda_r \vec{\nabla} T], \tag{11}$$

  where $\vec{n}$ is the surface normal vector pointing from the wall towards the cavity, λ_r is the rock conductivity ($\mathrm{W.m^{-1}.K^{-1}}$) and $\vec{\nabla} T$ is the temperature gradient in the embedding rock at the interface with the gas phase.

- The convective flux is given by the Newton law, cf. equation 6.

- The net radiative flux is the difference between the emitted and absorbed fluxes. It depends on the wall geometry, radiative properties and temperature. Assuming gray and diffuse surfaces, the following expression is obtained

$$\varphi_{rad} = \epsilon(\sigma T^4 - E), \tag{12}$$

  where ϵ is the surface emissivity, $\sigma = 5.67 \times 10^{-8} \mathrm{W.m^{-2}.K^{-4}}$ is the Stefan-Boltzmann constant and E is the irradiation ($\mathrm{W.m^{-2}}$) [35]. The determination of E is not trivial, as it must take into account the geometry of the cavity through the view factor evaluation (for instance, some part of a wall may be hidden in case of overhangs). The computation of surface-to-surface radiations is based on the radiosity method.

- The last term concerns the heat flux induced by evaporation or condensation on the wall,

$$\varphi_w = L\rho_w v_{ev}, \tag{13}$$

where L is the latent heat ($\mathrm{J.kg^{-1}}$).

3. Thermophysical properties

For the conductivity and diffusivity of the limestone embedding rock, we used $\lambda_r = 1.656\ \mathrm{W.m^{-1}.K^{-1}}$, $a_r = 8.10^{-7}\,\mathrm{m^2.s^{-1}}$ (estimated from data of the region of Lascaux in France, cf. Appendix B), in line with values used in similar karst environments [17, 18]. For air in the cavity, the following data are used: $\rho_a = 1.23\ \mathrm{kg.m^{-3}}$, $c_a = 1005\ \mathrm{J.kg^{-1}.K^{-1}}$, $\lambda_a = 0.025\ \mathrm{W.m^{-1}K^{-1}}$ (data for $T = 12^o$C [36, 34]). For water, density ρ_w is $999.5\,\mathrm{kg.m^{-3}}$ and latent heat of vaporisation L is $2473.10^3\mathrm{J.kg^{-1}}$ (data for $T = 12^o$C [37, 34]). The diffusivity of vapor in air D_w is $2.43\ 10^{-5}\,\mathrm{m^2.s^{-1}}$ [32]. Temperature variations in the cavity being small, the variation of the saturated vapor pressure with temperature may be assumed linear. Linearization around the mean temperature ($T_m = 12^o$C) leads to the following expression (obtained using data from [38]):

$$P_{sat}(T) = a_1 + a_2(T - T_m), \tag{14}$$

with $a_1 = 1402.6\,\mathrm{Pa}$, $a_2 = 92.49\,\mathrm{Pa.K^{-1}}$.

The emissivity ϵ is close to one for limestone or water for infrared radiation (0.95 and 0.96, respectively, [39]). As shown in the following, simulations performed for ϵ varying in the interval $[0.9, 1]$ led to very similar temperature fields. We thus keep $\epsilon = 1$ in the following to model radiative transfer, except when explicitly mentioned.

As detailed in Appendix A, an estimation of the thermal boundary layer thickness, $\delta_T \sim 1$cm, was obtained from previous simulations of convection performed for Lascaux cave configuration [3]. Thus the order of magnitude of the heat and mass transfer coefficients are $h_{th} \sim \lambda_a/\delta_T \sim 2.5\,\mathrm{W.m^{-2}.K^{-1}}$ and $h_m \sim D_w/\delta_T \sim 0.0024\,\mathrm{m.s^{-1}}$. In the result section, we refer as the "wet reference case" the configuration of a cavity filled with humid air, using these values of heat and mass transfer coefficients and $\epsilon = 1$. The same configuration with $v_{ev} = 0$ is referred as the "dry reference case". To compare the magnitude of the different heat transfer modes (convection, radiation, phase

change), additional simulations are performed with different values of these parameters.

4. Time constants and humidity in the cavity

Interesting insights can be derived from consideration of model time scales. Equations 5 and 6 with the assumption of constant heat transfer coefficient h_{th} yields

$$\tau_a \frac{\mathrm{d}T_a(t)}{\mathrm{d}t} = \overline{T}(t) - T_a(t), \tag{15}$$

where $\tau_a = (M_a c_a)/(S\, h_{th})$ is the thermal time constant of air ($\tau_a \sim 14\,\mathrm{min}$ for the reference case) and

$$\overline{T}(t) = 1/S \iint_S T(x,z,t)\ \mathrm{d}S \tag{16}$$

is the average wall temperature at time t. Using orders of magnitude, one may compare the variation ΔT_a of the air temperature T_a during a given time Δt with the temperature difference $\overline{T} - T_a$. Injecting $dT_a/dt \sim \Delta T_a/\Delta t$ in equation 15 yields

$$\frac{\overline{T} - T_a}{\Delta T_a} \ \sim \frac{\tau_a}{\Delta t} \sim 10^{-5} \ll 1, \tag{17}$$

where $\Delta t \sim 1$ year has been considered (more rapid fluctuations are damped by heat diffusion in rock). Since the difference between the air temperature T_a and the average wall temperature $\overline{T}(t)$ is much lower than the amplitude of air temperature fluctuations in the cavity, we can do the approximation

$$T_a(t) \simeq \overline{T}(t). \tag{18}$$

Equations 18, 16 and 6 lead to

$$\iint_S \varphi_{conv}\ \mathrm{d}S\ \simeq 0. \tag{19}$$

The convective heat flux at the cavity wall is thus conservative (the variation of the internal heat stored in the air can be neglected compared with the heat transferred to – or released from – the walls by convection).

The same derivation can be done for the vapor transfer. From equations 7 and 8 and with the assumption of constant mass transfer coefficient h_m, we get

$$\tau_w \frac{\mathrm{d}c_w}{\mathrm{d}t} = \overline{c_{sat}}(t) - c_w(t), \tag{20}$$

where $\overline{c_{sat}}(t) = 1/S \iint_S c_{sat}(x,z,t)\ \mathrm{d}S$ is the average vapor concentration at the wall. The time constant of the vapor transfer reads $\tau_w = V_{cave}/(S\,h_m)$ ($\tau_w \sim 12\,\mathrm{min}$ for the wet reference case). The same analysis as previously done for heat transfer yields

$$c_w(t) \simeq \overline{c_{sat}}(t) \quad \text{and} \quad \iint_{\mathrm{S}} \varphi_{\mathrm{w}}\ \mathrm{dS} \simeq 0. \tag{21}$$

The concentration of water vapor in the gas phase can be approximated by the average concentration at the walls, and the flux of water vapor due to evaporation and condensation is conservative (the variation of the mass of water stored in the humid air of the cavity is negligible compared with the water condensed – or evaporated – at the walls).

Another consequence of the model assumptions for the wet configuration is that the humidity Hr remains close to 1. Indeed, the variations of temperature in the cavity being small, c_{sat} in equation 9 may be approximated by $c_{sat} \simeq P_{sat}(T)\ M_w/(R\,\overline{T})$ (because $(T-\overline{T})/\overline{T} \ll 1$). Using this approximation and equations 14, 18 and 21 we get $c_w \simeq c_{sat}(T_a)$ and

$$H_r = c_w/c_{sat}(T_a) \simeq 1. \tag{22}$$

Numerical simulations confirm these results, which are typical of a non-ventilated and humid cavity.

5. Numerical method

Evaluation of heat and mass transfer in the domain $\mathcal{D} = \mathcal{M} \cup \mathcal{C}$ requires to solve equations 1 to 10.

The finite element commercial software Comsol Multiphysics (Galerkin method) was used to perform numerical simulations. The Comsol "Heat Transfer modulus" takes over the different modes of heat transfer, including the computation of surface-to-surface radiations, based on the radiosity method. An irregular mesh was used (with a total of about 11200 Lagrangian quadratic elements). The mesh was refined close to the top surface and in the vicinity of the cavity.

We checked that using a more refined mesh did not change the results. Several tests were also performed to ensure that: (i) the local energy balance holds (equation 10), (ii) the spatial average of the net radiative flux is quasi zero at any time (less than $\pm 2 \times 10^{-5}\mathrm{W/m^2}$), (iii) the spatial average of φ_{conv} and φ_w are both close to zero (less than $\pm 2 \times 10^{-4}\mathrm{W/m^2}$ for the wet reference

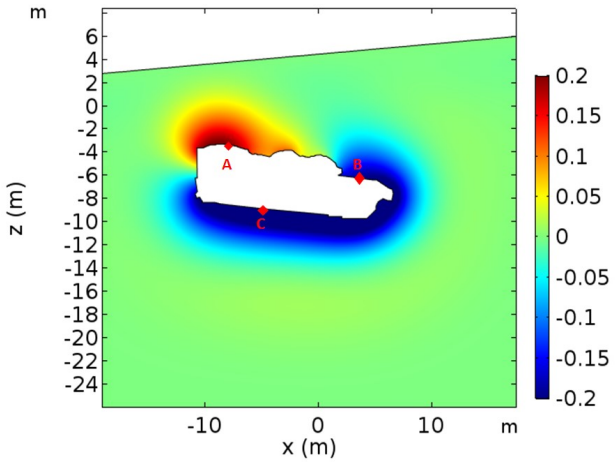

Figure 2: Difference of the temperature fields (color scale on the right in °C) with and without cavity in July. The cavity modifies the karst massif temperature field on a distance of a few meters.

case, cf. equations 19 and 21).

6. Results for a periodic yearly regime

A yearly periodic boundary condition is imposed at the ground surface (cf. equation 3),

$$T_{ex}(t) = T_m + (\Delta T/2)\ \cos(\omega t), \tag{23}$$

where $\omega = 2\pi/\tau$. The period τ is one year. The mean temperature, T_m, is set to 12°C and $\Delta T = 16$°C is the total amplitude of temperature variations.

The simulation is started with a uniform temperature equal to T_m in all the computational domain $\mathcal{M}$, and a vapor concentration in the cavity corresponding to a humidity of 100% at T_m. After a transient regime of a few years (not presented in this section), the cavity reaches a periodic yearly regime. Results presented in the following depict this periodic regime and time evolution of the variables are drawn for two periods, i.e. 24 months. The highest external temperature corresponds to $t = 0$, τ, 2τ (cf. equation 23). We assign the highest external temperature to July and January is therefore the month with the lowest external temperature.

6.1. Spatial distribution and time evolution of the temperature field

First of all, it is interesting to analyze the perturbation induced by the cavity on the temperature field of the karst massif. An illustration is given in Figure 2 which shows the difference between the solution with and without cavity for $t = \tau$. In the absence of cavity, heat transfer in the massif is purely conductive in our model. For the yearly periodic regime, and with the depth of our computational domain ($H = -40\,\mathrm{m}$), it can be shown that the solutions corresponding to a semi infinite medium or to an adiabatic boundary condition at $z = H$ are almost identical [40]. If we consider a 1D propagative thermal wave from the surface, the analytical solution in the case of a semi infinite medium is

$$T(d,t) = T_m + \frac{\Delta T}{2}\ \exp\left(-\sqrt{\frac{\omega}{2a_r}}d\right)\ \cos\left(\omega t - \sqrt{\frac{\omega}{2a_r}}d\right)\ , \tag{24}$$

where d is the distance along the normal to the ground surface ($d = d_v\,\cos\theta$). The amplitude of temperature variations decreases strongly with depth, due to the exponential term. Indeed $\sqrt{\omega/2a_r} = 0.35\,\mathrm{m}^{-1}$ for a period of one year and thus the attenuation factor is $\exp(-0.35\,d)$. The distance d to the ground surface of the three points A, B and C are 7.02 m, 10.87 m and 12.92 m, respectively. Thus the attenuation factors without cavity are 0.084, 0.022 and 0.01, respectively. While the oscillation amplitude of the external temperature T_{ex} is $\pm 8^{\circ}$C (cf. equation 23), it drops to $\pm 0.67^{\circ}$C for point A, and to $\pm 0.08^{\circ}$C for point C. The phase shifts for the three points A, B and C is 4.7 months, 7.3 months and 8.7 months, respectively (see Figure 3(a)). If the cavity is taken into account, results are very different as illustrated in Figure 3(b) which shows the time evolution of the temperature of the three fictive sensors A, B and C with cavity for the wet reference case (as defined in section 3). The amplitude of oscillation for point A, the closest to the ground surface, is $\pm 0.36^{\circ}$C when the cavity is present, versus $\pm 0.67^{\circ}$C without cavity. The time corresponding to the temperature maximum is only slightly modified by the presence of the cavity. The effect of the cavity is much stronger for points B and C for which temperature are now close to each other and close to the temperature of point A. Indeed, the maximum of the temperature difference $T_A - T_C$ drops from $\pm 0.72^{\circ}$C without cavity to $\pm 0.08^{\circ}$C with cavity. As a conclusion, convective and radiative heat transfers inside the cave homogenize the wall temperature significantly. Another illustration of the strong homogenisation of temperature induced by the cavity is given in Figure 4. The position on the wall is defined in terms of the curvilinear abscissa s(x,z) (see scheme in Figure 4). The spatial distributions of the temperature all along the cavity wall are compared for the configuration with and without cavity, for $t = 4$ months, which corresponds to November.

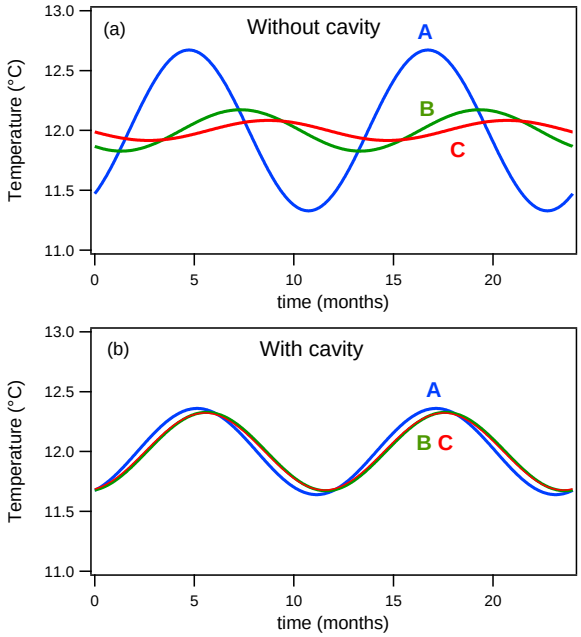

Figure 3: Time evolution (two periods) of the temperature of the three fictive sensors A (blue solid line), B (green solid line) and C (red solid line). (a): case without cavity, (b): cavity for the wet reference case ($t = 0$ corresponds to july, the month with the highest external surface temperature, cf. equation 23). The cave strongly homogenizes the temperature distribution compared to the purely conductive case (without cavity).

The spatial distribution of temperature along the cavity wall throughout the year is given in Figure 5 for the configuration with cavity and for the wet reference case. The external temperature being a cosine function with a one year period, and the model being quasi-linear, we get $T(s,t) - T_m \simeq -[T(s,t+\tau/2) - T_m]$ with $\tau/2 = 6$ months. Spatial variations are maximal around November and May, with $T_{max} - T_{min} \simeq 0.17$°C. July and January show the smallest spatial temperature variations. Note that due to the phase shift with external temperature, the seasons are quasi reversed for the cavity compared to the external temperature. July and January are the coldest and warmest months, respectively.

In conclusion, the presence of a cavity significantly affects the spatial repartition of temperature. The solution corresponding to the pure conductive problem obtained without cavity is thus a poor approximation of the wall temperature distribution, especially for the temperature of the cave floor.

6.2. Relative contributions of the heat transfer modes in the cavity

To go further in the characterization of heat and mass transfer, we analyze the relative contributions of the different transfer mechanisms, first for the dry configuration (comparison of radiative and convective heat transfer) and then introducing evaporation/condensation phenomena.

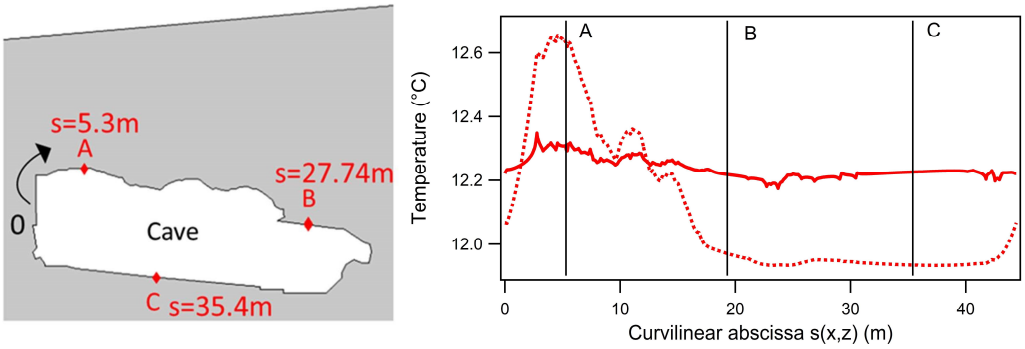

Figure 4: left: Scheme of the curvilinear abscissa $s(x, z)$. The origin of curvilinear abscissa corresponds to the middle height of the left part of the wall and the distance to the origin is covered clockwise - right: spatial distribution of temperature along the wall in November, for the configuration with cavity (wet reference case, red solid line) and without cavity (red dotted line). The position of the three sensors A, B and C is indicated by vertical lines. The spatial variation of temperature is significantly reduced by the presence of the cave.

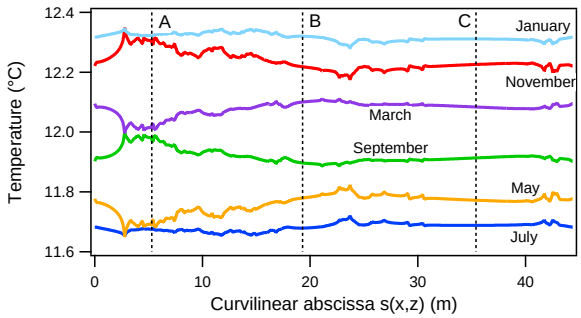

Figure 5: Spatial distribution of temperature along the cavity wall over the year, for the wet reference case. The position of the three sensors A, B and C is indicated by vertical lines. The spatial variations of temperature along the cavity wall vary from month to month, and are maximum in May and November.

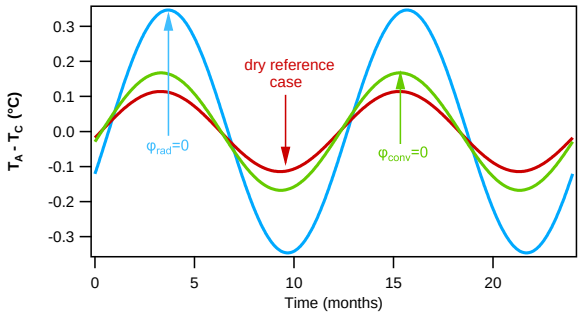

Figure 6: Difference between the wall temperature at points A and C, $T_A - T_C$, for different configurations: dry reference configuration (red solid line, $h_{th} = 2.5\,\mathrm{W.m^{-2}.K^{-1}}$ and $\epsilon = 1$), non radiative dry configuration (blue solid line, $\varphi_{rad} = 0$) and non convective dry configuration (green solid line, $\varphi_{conv} = 0$). Both radiative and convective heat transfer modes play an important role in the temperature homogenisation, the stronger impact coming from radiative heat transfer.

case	φ_{rad}	φ_{conv} h_{th} in $\mathrm{W.m^{-2}.K^{-1}}$	φ_w h_m in $\mathrm{m.s^{-1}}$	$\max(\mathrm{T_A - T_C})$ °C
1. (dry ref. case)	$\epsilon = 1$	$h_{th} = 2.5$	0	0.11
2.	0	$h_{th} = 2.5$	0	0.35
3.	$\epsilon = 1$	0	0	0.17
4.	$\epsilon = 1$	$h_{th} = 0.1$	0	0.16
5.	$\epsilon = 1$	$h_{th} = 1$	0	0.14
6.	$\epsilon = 1$	$h_{th} = 10$	0	0.06
7. (wet ref. case)	$\epsilon = 1$	$h_{th} = 2.5$	$h_m = 0.0024$	0.08
8.	$\epsilon = 0.9$	$h_{th} = 2.5$	0	0.12
9.	$\epsilon = 0.9$	$h_{th} = 2.5$	$h_m = 0.0024$	0.08

Table 1: Maximal value of the difference $T_A - T_C$ for different cases. The expression of radiative, convective and phase change fluxes are given in equations 12, 6 and 13, respectively.

6.2.1. Dry reference case

In order to assess the relative contribution of convective and radiative transfer, Figure 6 compares the temperature difference between sensors A and C for the following three configurations: (i) dry reference configuration (convective and radiative heat transfer with $h_{th} = 2.5\,\mathrm{W.m^{-2}.K^{-1}}$ and $\epsilon = 1$), (ii) non radiative dry configuration (convective heat transfer only, $\varphi_{rad} = 0$) and (iii) non convective dry configuration (radiative heat transfer only, $\varphi_{conv} = 0$). These three configurations correspond to cases 1, 2 and 3 in Table 1. Radiative heat transfer, which is always present in a cave, has a stronger impact than the convective heat transfer and leads to temperature difference of $\pm 0.17^{\circ}$C without convection, and to $\pm 0.11^{\circ}$C when both radiative and convective heat transfers are active.

As specified in the modeling section, the estimation of convective heat transfer is based on constant coefficients that do not take into account the various regimes of convection occurring throughout the year. Moreover, we only have orders of magnitude for these coefficients. Staying within the framework of this simplified model, we analyze the influence of the convection magnitude by performing new simulations with the following values: $h_{th} = 0$, 0.1, 1, $10\,\mathrm{W.m^{-2}.K^{-1}}$. The highest value, $h_{th} = 10\,\mathrm{W.m^{-2}.K^{-1}}$, can reasonably be considered as an upper bound for the studied configuration. All these simulations take into account radiative transfer. The maximal value of $T_A - T_C$ as a function of h_{th} is reported in Table 1, cases 1 and 3 to 6. Results for $h_{th} = 0.1\,\mathrm{W.m^{-2}.K^{-1}}$ and $h_{th} = 0$ are similar and correspond to the case where temperature homogenisation is ensured by radiative heat transfer only. As can be seen, increasing convective heat transfer coefficients result in a decrease of the amplitude of temperature variations which drops from $\pm 0.17^{\circ}$C when only radiative transfer is active to $\pm 0.06^{\circ}$C for $h_{th} = 10\,\mathrm{W.m^{-2}.K^{-1}}$.

The influence of ϵ in the range expected for limestone ($\epsilon > 0.9$) is small, about 0.01°C on the maximal value of $T_A - T_C$ when ϵ decrease from 1 to 0.9 (cf. cases 1 and 8 in Table 1).

6.2.2. Wet reference case

When evaporation and condensation are taken into account, phase change tends to decrease the difference between the wall and air temperatures. Indeed condensation, which occurs when the wall is colder than the air, is exothermic and thus heats the wall. The reverse is expected for evaporation. As a consequence, the spatial variations of temperature are smoothed when phase change occurs. For instance, Table 1 compares the maximal value of $T_A - T_C$ for the dry reference

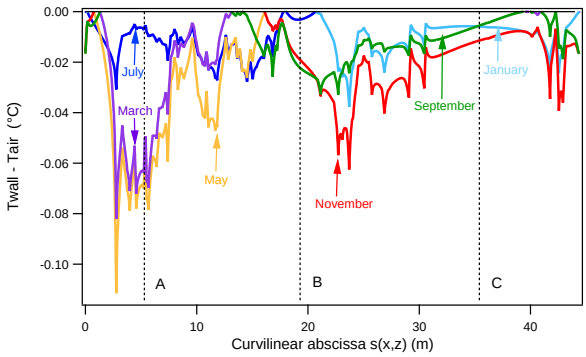

Figure 7: Spatial distribution of the temperature difference between the wall and air in the cavity for the wet reference case. Only negative values are reported on the graph, corresponding to the configuration suitable for condensation on the wall. The position of the three sensors A, B and C are indicated by vertical lines. Magnitude and period of condensation strongly depend on the spatial location.

configuration (case 1) and the wet reference configuration (case 7) : $T_A - T_C$ decreases from 0.11°C to 0.08°C when shifting from the dry to the wet reference cases.

In conclusion, radiative transfers cause a significant homogenisation of wall temperature. This effect is strengthened when convection or phase change are active. In the configuration considered in this study, the spatial variations of the wall temperature are of the order of 0.1°C.

As said in the modeling section, the wet reference case corresponds to a case without limitation of water supply, i.e. there is a permanent water film on the wall. Thus this configuration maximises the condensation or evaporation time durations. Though small, the temperature differences between wall and air are high enough to cause significant fluxes of evaporation ($T_{wall} - T_a > 0$) or condensation ($T_{wall} - T_a < 0$). The temperature difference between wall and air for the configuration suitable to condensation is given in Figure 7. Condensation is observed mainly in March and May at the upper part of the cave roof (point A), while it is observed in November in the lower part of the cave roof (near point B at $s \sim 23\,\mathrm{m}$). The temperature difference is smaller at the cave floor (point C). The evaporation rate throughout the year is shown in Figure 8 for the three probes. The model shows that periods of several consecutive months of significant condensation (or evaporation) may be observed on the same part of the wall (cf. for instance sensor A in Figure 8, for which the condensation rate is greater than 2μm/day for about five months). Depending on the location in the cave, this may produce a few tenth of millimeter of water on the cave walls. This result is important as some phenomena occurring on the wall (carbonate dissolution [41], clay swelling ...) may be strongly sensitive to the flow rate of condensation water. In order to get an upper bound of condensation fluxes, an additional simulation was performed using an estima-

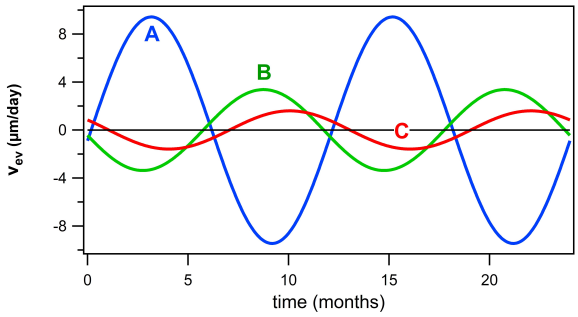

Figure 8: Time evolution of the evaporation rate v_{ev} (in μm/day) for the wet reference configuration, for sensor A (blue solid line), B (green solid line) and C (red solid line). By convention, v_{ev} is positive for evaporation and negative for condensation. Succession of condensation and evaporation periods of several months are observed.

tion of the upper bounds of these coefficients, that is four times the values of the wet reference case: $h_{th} = 10\,\mathrm{W.m^{-2}.K^{-1}}$ and $h_m = 0.0096\,\mathrm{m.s^{-1}}$. The evaporation rate is thus higher, close to $\pm 14\,\mu$m/day for sensor A.

The orders of magnitude of condensation rates are similar to experimental estimations performed in other caves: in the Kartchern cave in Arizona, Buecher [42] reports a condensation rate which varies from 0 to about 15μm/day during the year. Measurements performed in the Glowworm cave in New Zealand by De Freitas and Schmekal [22] in the Banquet Chamber gives values from 0 to about 12μm/day, when the Chamber was isolated from outside by a door.

The time evolution of the four different fluxes involved at the cave wall (conductive, convective, radiative and phase change) are given in Figure 9 for the wet reference case and for the three sensors. Due to the underlying assumptions (periodic boundary condition at the ground surface, zero flux at the bottom of the karst massif, quasi linear model), the fluxes at a given point are also periodic with a zero mean value. Depending on the location on the wall, they can be inphase (for instance sensors A and C) or shifted (sensor B). Their magnitude depends also on the sensor location. The highest fluxes are observed as expected at sensor A which is closer to the ground surface. Very few evaporation/condensation phenomena ($\varphi_w \simeq 0$ throughout the year) are observed on the cave floor (sensor C). It is interesting to note that succession of wet and dry periods is a known phenomenon that may be observed on some cave walls, including Lascaux cave. It would be interesting to compare simulations to observed time and spatial evolution of wall humidity. However such a comparison would require to shift to a more realistic 3D geometry.

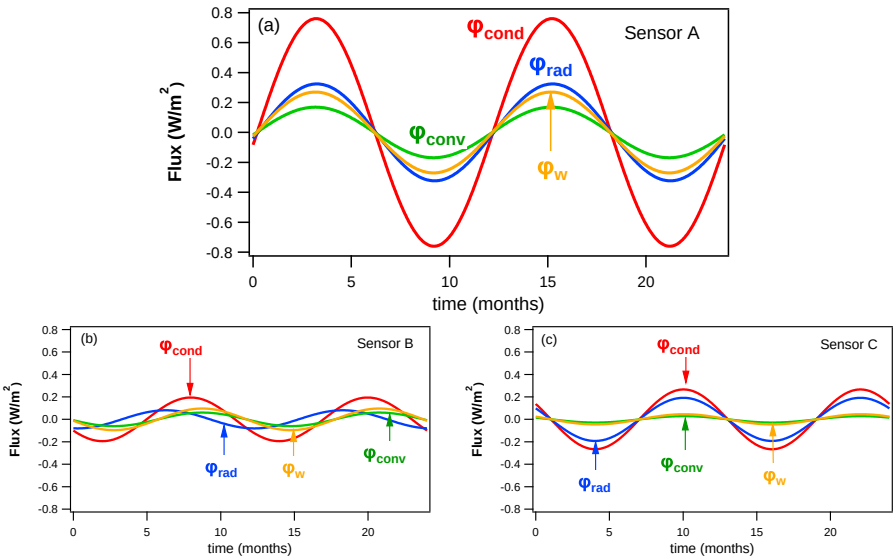

Figure 9: Time evolution of the different fluxes for the wet reference case, for sensors A (a), B (b), C (c). At any time, the conductive flux (red solid line) is the sum of the convective flux (green solid line), radiative flux (blue solid line) and evaporation/condensation flux (orange solid line). The highest fluxes are observed at sensor A which is closer to the ground surface than sensors B and C.

6.2.3. Influence of the geothermal flux

As observed in Figure 9 the fluxes are weak, less than $1\,\mathrm{Wm}^{-2}$. However, the maximal values of the conductive flux at the wall are much greater than the geothermal flux that has been neglected in our model. Indeed the conductive flux corresponding to a gradient of 3°C/100 m would be about $0.05\mathrm{Wm}^{-2}$. A simulation was performed by imposing a constant flux of $0.05\mathrm{Wm}^{-2}$ at the bottom of the computational domain ($z = H$). The mean yearly temperature in the massif is therefore no more equal to the mean external temperature ($T_m = 12$°C) and increases with depth. Without cavity, it increases from 12.21°C for sensor A to 12.39°C for sensor C. With the cavity and for the wet reference case, homogenisation induced by the cavity results in a mean yearly temperature of 12.31°C for sensor A and 12.32°C for sensor C. The geothermal flux does not change much the magnitude of the cavity wall temperature spatial repartition, compared to the adiabatic case considered in the previous sections. Indeed, $T_A - T_C$ varies from -0.09°C to 0.07°C during one year, while it is between ± 0.08°C for the adiabatic case. This validates the approximation of zero flux used as boundary condition at the bottom of the karst massif in most of the simulations of the periodic yearly regime, as soon as the present study concerns the analysis of the main trends of heat and mass transfer in a shallow cavity.

7. Simulations with real climatological data

7.1. Available data

Simulations of the thermal response of the cave are performed using real meteorologic data for the temperature boundary condition imposed at the surface of the massif (equation 3). To get a long period of available measurements, we used the data of Gourdon's weather station ($44^o44'42''$N, $1^o23'48''$E), located at a distance of about 150 km from Lascaux ($45^o3'14''$N, $1^o10'3''$E). The altitudes are 260 m and 185 m for Gourdon and Lascaux, respectively. The data of the two locations are correlated [43], but the temperature recorded at Lascaux is often lower. The monthly average external temperatures in Gourdon for the period 1941-2017 were provided courtesy of "Météo-France" and are displayed on Figure 10 (a). These monthly data were used to compute the yearly average temperature (Figure 10 (b)). The lowest yearly average temperature is observed in 1956 (10.9°C) and the highest in 2011 (14°C). A slight warming trend may be observed during about the last thirty years. The fluctuation amplitude over one year, corresponding to the difference between the hottest and coldest months for each year, is given in Figure 10 (c). It varies a lot from one year to another, for instance 12.6°C in 2002 and 22.7°C in 2012.

7.2. Influence of the initial state and boundary condition

Unlike for the yearly periodic regime, the choice of the initial temperature field and of the boundary condition at the bottom of the computational domain is challenging for simulations with real data containing temperature variations over long time scales (e.g. decanal temperature variations). Indeed, for the yearly periodic regime studied in section 6, the depth of the computational domain ($H = -40\,\mathrm{m}$) was large enough to be insensitive to yearly fluctuations. The mean temperature $T_m = 12°\mathrm{C}$ was chosen as initial condition for the whole domain. As this value remained the same from one year to the next, the effect of the initial condition was sensitive over a few years only and the periodic regime was rapidly achieved.

This is no longer the case with real data as the yearly average temperature shows potentially long-term temporal variations. Therefore, fluctuations of the temperature field can penetrate deeper in the karstic massif. In addition the temperature field inside the massif at the beginning of the data set (1941) is unknown and results from the prior thermal history. Thus a sensitivity analysis was performed in order to evaluate the impact of the initial condition and bottom boundary condition on simulations with real meteorologic data. Three scenarios have been tested: (i) The first scenario

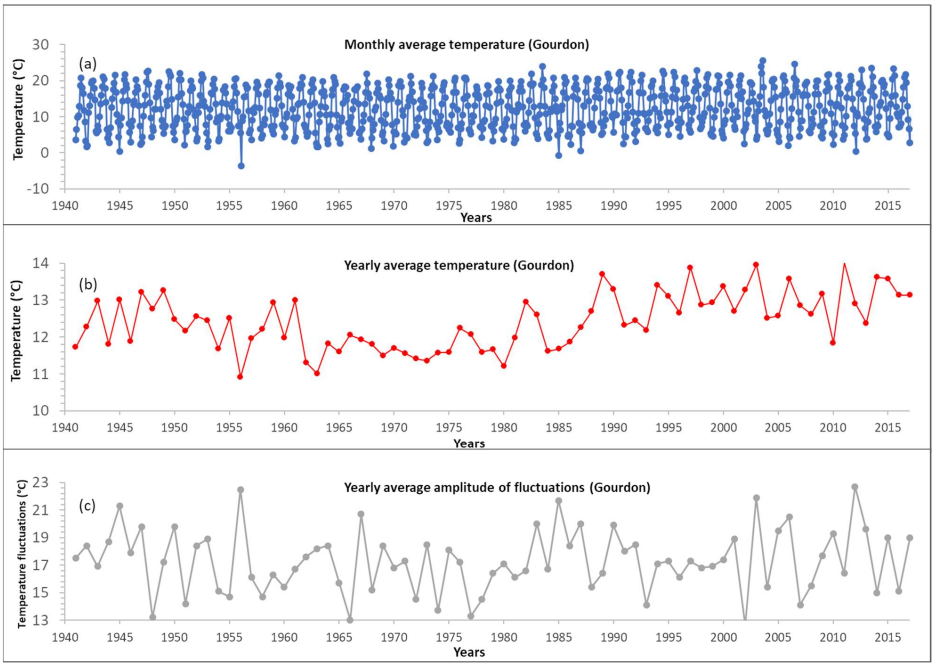

Figure 10: Gourdon's weather station. (a): monthly average external temperature. (b): yearly average external temperature (c) yearly amplitude of fluctuations estimated from monthly average temperature (difference between the hottest and coldest months for each year).

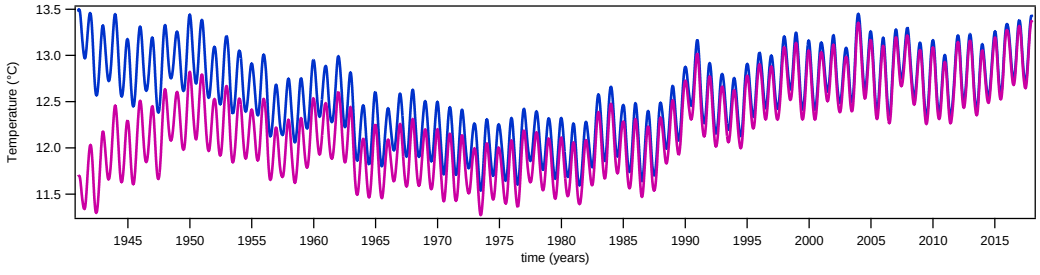

Figure 11: Simulations of the time evolution of the temperature at point A for the wet reference case and scenario (i) with two initial conditions: $T = 11.7^{o}$C (magenta continuous line) and $T = 13.5^{o}$C (blue continuous line). Due to the large time constant of the diffusive massif, a few decades are needed to make the signal independent on the initial condition.

corresponds to the configuration used in most of the previous simulations, with a zero flux boundary condition at $z = H = -40\,\mathrm{m}$. The initial condition is assumed uniform in the massif, and two values have been tested. One is 11.7°C, which is the average temperature for the year 1941, corresponding to one of the lowest observed on the available times series. Another one is 13.5°C, which belongs to the highest observed values. (ii) In the second scenario the zero flux boundary condition is imposed at greater depth, at $z = -100\,\mathrm{m}$. (iii) In the third scenario, a constant flux of $0.05\mathrm{Wm}^{-2}$ (geothermal flux) is imposed at $z = H = -40\,\mathrm{m}$. For this third scenario, the initial temperature is set to 11.7°C or 13.5°C at the ground surface, and increases linearly with depth. For all the tests, the 77 years of Gourdon's data have been used as boundary condition at the ground surface, and the parameters are those of the wet reference case.

For the first scenario, Figure 11 shows the time evolution of the temperature at point A for the two different initial conditions. As can be seen, the initial condition affects the results over a long period. About fifty years of simulation are needed for the gap between the two simulations to become lower than 0.25 °C. The slow increase of the average temperature observed during the period 1988-2017 is correlated with the behavior of the external temperature.

The influence of the initial condition needs more time to disappear in the second scenario as a larger depth is involved, and the difference on T_A with the two initial conditions is still 0.38 °C in 1990 (results not shown here). Figure 12 gathers the results of the six tests (3 scenarios and two initial conditions) for the temperature at point A for the last fourteen years. As can be seen, the general time evolution is the same for all the tests. For instance, the existence of a warmer year in the cavity in 2007 is obtained for all the simulations. But the discrepancy on the temperature value between the six tests is rather large, about 0.4 °C between the two extreme configurations. This value is of the same order as the amplitude of temperature variations between winter and summer, from 0.5 °C to 0.9 °C depending on the year.

However, the uncertainty on the initial temperature and the boundary condition affects only slightly the temperature difference along the cavity wall. Figure 13 shows the difference $T_A - T_C$ for the six tests along the last fourteen years. The amplitude of variation of $T_A - T_C$ varies from about 0.12°C to 0.16°C (depending on the year) for all the tests. These values are close to the one obtained in the yearly periodic case. Indeed, even if the annual temperature fluctuations at Gourdon change from one year to another (Figure 10 (c)), their average value is close to the amplitude of the external temperature in the yearly periodic regime (16°C, cf. equation (23)).

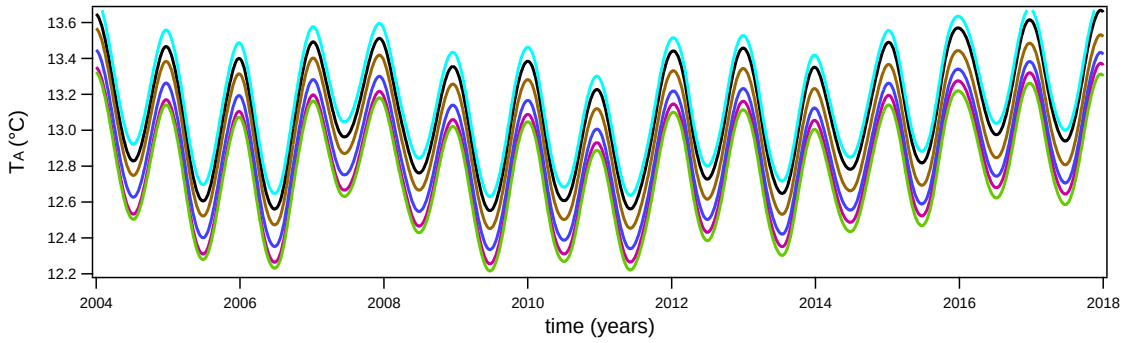

Figure 12: Simulations of the temperature T_A for the three scenarios and two different initial conditions. From top to bottom: scenario (iii) with $T = 13.5$°C (light blue continuous line), scenario (iii) with $T = 11.7$°C (black continuous line), scenario (ii) with $T = 13.5$°C (brown continuous line), scenario (i) with $T = 13.5$°C blue continuous line), scenario (i) with $T = 11.7$°C (magenta continuous line), scenario (ii) with $T = 11.7$°C (green continuous line). The general trend is the same for all the tests, but significant differences on the temperature are observed between the different tests.

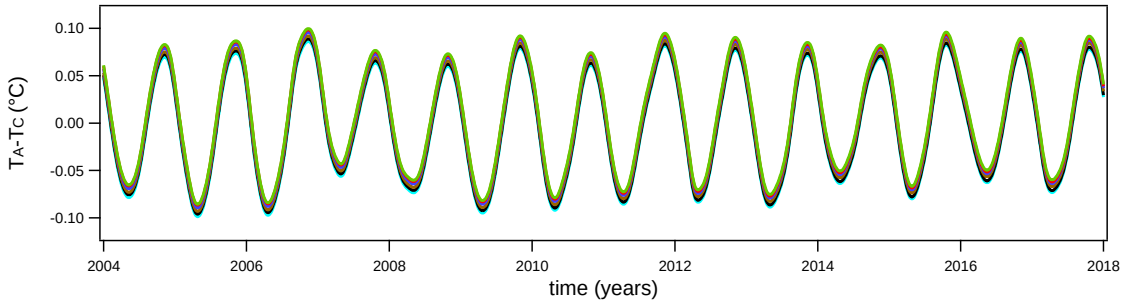

Figure 13: Simulations of the temperature difference $T_A - T_C$ for the three scenarios and two different initial conditions: scenario (iii) with $T = 13.5$°C (light blue continuous line), scenario (iii) with $T = 11.7$°C (black continuous line), scenario (ii) with $T = 13.5$°C (brown continuous line), scenario (i) with $T = 13.5$°C blue continuous line), scenario (i) with $T = 11.7$°C (magenta continuous line), scenario (ii) with $T = 11.7$°C (green continuous line). The six curves are very close, which means that the difference $T_A - T_C$ is little sensitive to the initial conditions in the massif.

As a conclusion, due to the uncertainty on the thermal history of the massif, the model does not provide an accurate estimate of the wall temperature at a given point. However, it gives information on global climatological trends in the cavity and on the spatial variations of wall temperature, which is an important point to estimate evaporation/condensation rate. Finally, for future studies, these results underline the importance of deepening the knowledge of heat transfer in karst massif to improve the choice of a pertinent boundary condition.

7.3. Comparison with Lascaux cave data

The geometry used in our simulations (2D closed cavity) is a simplified scheme of the real passage in Lascaux cave ("the Hall of Bulls"). Several other simplifying assumptions have also been made, so that the results analysed in the previous sections may be viewed as extreme cases of

the real configuration. Indeed, the cavity is assumed to be closed, despite the fact that exchanges with lateral passages exist seasonally, as evidenced by the analysis of the space and time evolution of the CO_2 pressure recorded in several locations in the cavity [43, 41]. Small exchanges with the outdoor air may also occur. Using external temperature data as boundary condition for the ground temperature is also an approximation, and a more realistic simulation would require to take into account sunshine, inhomogeneity in the ground vegetation cover etc (cf. for instance [44, 45, 46]). However, as we only focus on the main characteristics of the climate in the cavity, it is anyways interesting to compare simulations with field data, to see to what extend the general trends obtained with our model are observed in the real cavity and to what extend the simplified conditions considered in the simulations reflect the thermal behavior of the cavity.

We use experimental data of two sensors located on the ceiling and floor of the Hall of Bulls, approximately in the middle of the Hall.

Temperature simulations at point A and C (scenario (i) with $T = 11.7$°C as initial condition) and measured temperature at the ceiling and floor sensors are displayed in Figure 14. Simulated temperatures follow very well the general trend of the experimental data. For instance the warmer years 2007 and 2008 are observed both in simulated and experimental temperatures, and the increase of the average temperature observed during the last four years is also obtained in the simulations. This means that the diffusive equation used to model heat transfer in the embedding rock is suitable for Lascaux cave. Experimental temperatures are lower than the simulated ones, which may be partly due to the uncertainty on the initial state (cf. section 7.2) and partly to the differences between Gourdon and Lascaux external temperatures in recent years. Indeed average yearly external temperatures recorded at Lascaux from 2012 to 2017 are for instance about 0.7°C lower than those of Gourdon.

As can be seen, simulations overestimate the seasonal temperature fluctuations, which are about 0.6°C between summer and winter for point A, while they are of the order of 0.4°C for the ceiling measured temperatures. Simulations also underestimate the temperature difference between the roof and ceiling: the temperatures of the two points A and C (magenta and gray lines) are very close to each other, compared to the measurements at the ceiling and floor (green and brown dots).

This is due to the simplified assumptions (geometry and air description) used in the model. First, one may expect that radiative heat transfers are slightly overestimated in the 2D model used in the simulations. The real cavity is indeed 3D, with a more tortuous geometry than the one

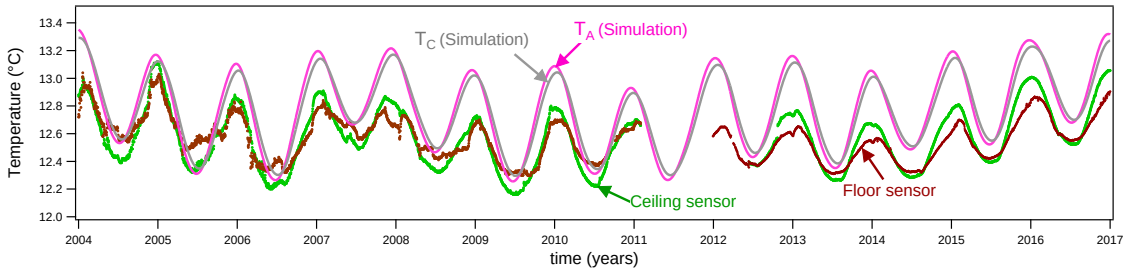

Figure 14: Comparison between simulations (scenario (i), $T = 11.7^{o}$C) and Lascaux cave measurements: simulated T_A (magenta solid line), simulated T_C (gray solid line), Lascaux ceiling measurements (green dots), Lascaux floor measurements (brown dots). The main trends are well reproduced by the model, however we observe lower seasonal variations and higher temperature difference between the floor and ceiling in the real cavity, compared to the 2D simulations.

used in the simulations. The presence of side walls connecting the floor to the ceiling, and the complex geometry (some parts of the wall are not facing each other) will modify the magnitude and repartition of radiative heat transfer and will reduce the homogenisation of the temperature wall. A planned extension of the present model is thus to shift to a 3D geometry, close to the real cavity configuration.

A second point concerns the assumption of a unique air temperature, which means that air is thoroughly mixed, and the assumption of constant heat transfer coefficient. The challenge is to improve the description of convection, while maintaining a model light enough to allow long term simulations. For this purpose, preliminary simulations of air convection using Navier Stokes equations and coupling the cavity with the massif are planned, in order to characterize the seasonal evolution of natural convection in the cavity. The objective is to build a reduced model from the detailed simulations, closer to real configurations than the current model. For instance it may include heat and mass transfer coefficients that change according to each season or according to the location on the wall.

8. Conclusion and outlook

We have developed a coupled model of heat and mass transfer in a shallow and non-ventilated cave embedded in a karst massif. The model takes into account conductive transfer in the karst massif, convective and radiative transfer in the cavity and evaporation/condensation at the cavity wall. First simulations have been performed for a periodic Dirichlet condition at the ground surface and we analyzed the corresponding periodic regime in the cavity. Results demonstrate that the temperature field is significantly deformed compared to the case without cavity. Fluxes at cave

wall, related to radiation, air-convection and evaporation/condensation (in case of a humid cave) all contribute to a significant homogenization of wall temperatures, with an important contribution of radiative transfer, which can never be neglected. In case of high humidity, simulations of evaporation/condensation periods show that some parts of the wall may be durably (several months) subjected to significant condensation (or evaporation).

Real meteorological data, 77 years of external temperature data of the Gourdon station in France, have been used as input of the model. Results of simulations have been compared to experimental temperature of Lascaux cave, with good agreement considering the simplifying hypotheses assumed for this modeling. The asset of such a model is the low computing time required to simulate several years, and thus its ability to follow long time evolution. Further investigations are planned to improve the description of the temperature field while maintaining reasonable computing times, taking into account 3D geometry, seasonal changes in the convective regime and the ground vegetation cover.

The alternation of condensation and evaporation is a factor of wall weathering by calcite dissolution and precipitation. Humidity is furthermore a factor controlling ecosystems, leading to a specific microbiology associated to this environment, which in turns represents a further potential weathering agent. Concerning evaporation/condensation two configurations have been considered in the model, the dry reference case (no water in the cavity) and the wet reference case (without water limitation, i.e. there is always a water film on the wall). In this last configuration, the modeling shows that duration and intensity of condensation/evaporation events highly depend on the position of the spot considered on a cave wall. Two nearby areas on the wall may differ from a climatological and ecosystemic point of view. The present paper shows that the modeling of this pattern is complex, nevertheless possible. Indeed, in a real configuration, the cavity should be situated between the dry (no water) and wet (no limitation on water) reference cases. This may be taken into account in the model, provided that data on the availability of water throughout the year are known. This may be a complex problem, which requires the estimation (or the modeling) of the exchanges with the embedding rock (water percolating through the massif) or direct water exchanges with external air for which humidity changes during the year (cf. for instance the study of Li and co-authors [45, 46] where the heat and moisture transfer in the surrounding soil are considered).

Results significantly improve our understanding of conditions taking place in a shallow cavity,

what will help improving the management of caves, especially those with very fragile decorations such as Paleolithic paintings. It may also be useful for managing shallow underground constructions (e.g. a mine or even a cellar). For Lascaux cave, it will guide us to identify areas which are the most exposed to weathering and to test the effect of past and potential changes in nearby conditions. The modeling was focused on the case of a shallow and confined cave. In this situation heat is fully transferred from the surface to the cave through the rock-matrix. Results cannot be transferred directly to the case of a ventilated cave where heat is more significantly transferred by air circulation. Condensation and evaporation fluxes are expected to be even more important than in a confined cave, providing a clear motivation for expanding the modeling to other conditions.

Acknowledgments

The study is part of investigations supported by the French Ministry of Culture, Direction des Affaires Culturelles de Nouvelle-Aquitaine. We want to thank them and their sub-contractants for support and data. In this context we want to thank more specifically Jean-Christophe Portais and Sandrine Géraud for their help. We also thank Météo France which provided Gourdon's meteorological data within the framework of French research support.

Appendix A. Estimation of the convective heat transfer coefficient

The convective heat transfer coefficient is difficult to evaluate because it is a local quantity which depends on many parameters, including the global geometry of the system and the local surface morphology of the walls. The geometry of real caves is extremely complex, but as part of the simplified model developed in this paper, we can provide an order of magnitude of this coefficient.

A scale analysis of the heat flux transferred from a wall to the adjacent fluid [36] shows that the order of magnitude of the convective heat transfer coefficient, h_{th}, is

$$h_{th} \sim \frac{\lambda_a}{\delta_T} \tag{A.1}$$

where λ_a is the thermal conductivity of air ($\lambda_a = 0.025\,\mathrm{W.m^{-1}.K^{-1}}$) and δ_T is the thermal boundary layer thickness, i.e. the region in which the temperature changes from T_w at the wall to T_a far from the wall. In a convective heat transfer problem, the challenge is then to determine δ_T scaling, which depends on the characteristic parameters of the system. For air, the Prandtl number (i.e. the ratio between momentum and thermal diffusivities) is of order unity which means that δ_T is of the same

589 order as the velocity boundary layer thickness δ.

590 Air motion in a cave is mainly driven by the buoyancy effect due to the presence of density
591 variations between the different areas of the cave. A convection flow can develop on a large scale
592 (cave scale) which can be locally seen as a forced convection flow, for example in narrow passages,
593 or as a natural convection flow along the vertical walls in larger areas.

594 If the air flow is considered as a forced convection flow, the velocity boundary layer thickness δ,
595 i.e. the region in which the velocity changes from zero at the wall to u_∞ far from the wall, depends
596 on the Reynolds number, $\mathcal{R}e_L = u_\infty L/\nu_a$ with ν_a the kinematic viscosity of air ($\nu_a \sim 10^{-5}\,\mathrm{m^2.s^{-1}}$)
597 and L the characteristic length of the system. Numerical simulations performed by Malaurent at
598 al. [4] in the Lascaux cave show that the order of magnitude of the velocity in narrow passages
599 is 10 cm/s. By choosing $L \sim 1\,\mathrm{m}$, the characteristic length over which the wall of a cave can be
600 considered as flat, we obtain $\mathcal{R}e_L \sim 10^4$. The flow is therefore laminar ($\mathcal{R}e_L \lesssim 10^5$). Based on a
601 scale analysis of the terms involved in the momentum conservation equation of a forced flow along
602 a flat plate [36], we can estimate the order of magnitude of the laminar boundary layer thickness:

$$\delta \sim L\mathcal{R}e_L^{-1/2} \tag{A.2}$$

603 For $\mathcal{R}e_L \sim 10^4$ and $L \sim 1\,\mathrm{m}$, we obtain $\delta \sim 1\,\mathrm{cm}$ hence $\delta_T \sim \delta \sim 1\,\mathrm{cm}$.

604 If we now consider a natural convection flow, the air motion is generated by the difference in
605 density, $\Delta\rho$, between the air in contact with the wall and the air away from the wall. Let us assume
606 that this difference is induced by temperature variations only (thermal convection). The thermal
607 boundary layer thickness δ_T depends on the thermal Rayleigh number $\mathcal{R}a_L = g(\Delta\rho/\rho)L^3/(D_{th}\nu)$,
608 with g the gravitational acceleration and D_{th} the thermal diffusivity.

609 Considering $T_w - T_a \simeq 0,1\ ^\circ\mathrm{C}$, we estimate $\Delta\rho/\rho \sim 10^{-4}$. For a characteristic length scale
610 $L \sim 1\,\mathrm{m}$, $\nu \sim D_{th} \sim 10^{-5}\,\mathrm{m^2.s^{-1}}$, $g \simeq 10\,\mathrm{m.s^{-2}}$, we obtain $\mathcal{R}a_L \sim 10^7$. The flow is therefore
611 laminar ($\mathcal{R}a_L \lesssim 10^9$). Based on a scale analysis of the terms involved in the coupled momentum
612 and energy conservation equations of a natural convection flow along a vertical flat plate of height
613 L [36], we estimate the order of magnitude of the laminar boundary layer thickness for air:

$$\delta_T \sim L\mathcal{R}a_L^{-1/4} \tag{A.3}$$

For $\mathcal{R}a_L \sim 10^7$ and $L \sim 1\,\mathrm{m}$, we obtain $\delta_T \sim 1\,\mathrm{cm}$.

It is also possible to estimate the order of magnitude of the velocity in the boundary layer: $v \sim \sqrt{g(\Delta\rho/\rho)L} \sim 3\,\mathrm{cm/s}$. This value corresponds to the magnitude of the velocity calculated near the vertical walls of the "Hall of Bulls" reported by Malaurent at al. [4, 3]. Using helium filled balloons, Schoeller [30] made some estimations of the air velocity at the ceiling, and obtained values from about 6 cm/s to about 20 cm/s.

As a conclusion, for the two possible convection regimes the order of magnitude of the thermal boundary layer thickness is $\delta_T \sim 1\,\mathrm{cm}$, which yields to an estimation of the convective heat transfer coefficient using equation A.1 : $h_{th} \sim 2.5\,\mathrm{W.m^{-2}.K^{-1}}$.

It is important to be aware that the value given above for h_{th} is not a precise value but only an order of magnitude which reflects a very simplified description of the convection heat fluxes that occur in caves.

Appendix B. Estimation of the limestone rock diffusivity

The estimation of the rock diffusivity a_r is based on temperature measurements performed during about 22 months in the karst massif, a few tens of meters away from the Lascaux cave (provided courtesy of the technical staff of Lascaux cave). The sensors used for this purpose are located vertically inside the massif, at depths $z_1 = -1.5\,\mathrm{m}$, $z_2 = -2.3\,\mathrm{m}$, $z_3 = -3.2\,\mathrm{m}$ and $z_4 = -4\,\mathrm{m}$.

Assuming 1D conduction heat transfer between the four sensors, the temperature field in the domain $z_1 \geq z \geq z_4$ is described by the conduction equation

$$\frac{\partial T}{\partial t} = a_r \left(\frac{\partial^2 T}{\partial z^2} \right). \tag{B.1}$$

The temperatures of the two sensors located at $z_1 = -1.5\,\mathrm{m}$ and $z_4 = -4\,\mathrm{m}$ are used as Dirichlet boundary conditions at the frontier of the domain, for $0 \leq t \leq \Gamma$, with $\Gamma = 667$ days. The initial condition, $T(z, t = 0)$, is fitted by interpolation between the four sensors. With these initial and boundary conditions, the temperature field for $z_1 > z > z_4$ is obtained by solving equation B.1. The temperatures resulting from the simulation for the two sensor positions $z_2 = -2.3\,\mathrm{m}$ and $z_3 = -3.2\,\mathrm{m}$ and for $0 \leq t \leq \Gamma$, are noted $T_{sim2}(t)$ and $T_{sim3}(t)$.

Simulations are performed for different values of the diffusivity a_r. The value of a_r that will be adopted for the limestone massif is the one which minimizes the difference between the simulated values, $T_{sim2}(t)$ and $T_{sim3}(t)$, and the experimental data at the same depths, $T_{mes2}(t)$ and $T_{mes3}(t)$. To this end, the errors $ER2$ and $ER3$ are estimated by the following expressions

$$ER2(a_r) = \left[\frac{1}{\Gamma}\int_0^{\Gamma}(T_{sim2}(t) - T_{mes2}(t))^2 dt\right]^{1/2}, \tag{B.2}$$

which is approximated by

$$ER2(a_r) \simeq \left[\frac{1}{N}\Sigma_{i=1,N}(\tilde{T}_{sim2}(t_i) - \tilde{T}_{mes2}(t_i))^2\right]^{1/2} \tag{B.3}$$

with $t_i = i\delta t$ where δt is the sampling time and $\tilde{T}$ the average temperature over δt. At depths $z < z_1 = -1.5\,\mathrm{m}$, high frequency fluctuations of external temperature are filtered and we choose $\delta t = 24\mathrm{h}$. $\Gamma = N\delta t$, with $N = 667$.

The same procedure is performed for $ER3$. The figure B.15 gives the sum $ER2 + ER3$ as a function of the diffusivity a_r. The minimal value of the error is about $0.35^{\circ}\mathrm{C}$ and is obtained for $a_r \simeq 8 \times 10^{-7}\mathrm{m}^2.\mathrm{s}^{-1}$. It corresponds to $ER2 \simeq 0.15^{\circ}\mathrm{C}$ and $ER3 \simeq 0.2^{\circ}\mathrm{C}$. For this value of the diffusivity, Figure B.16 shows the simulated and measured temperatures for the two sensors. Given the uncertainty on the exact position of the sensors, the comparison between simulated and measured temperatures can be considered satisfactory and $a_r = 8 \times 10^{-7}\mathrm{m}^2.\mathrm{s}^{-1}$ is used in the simulations.

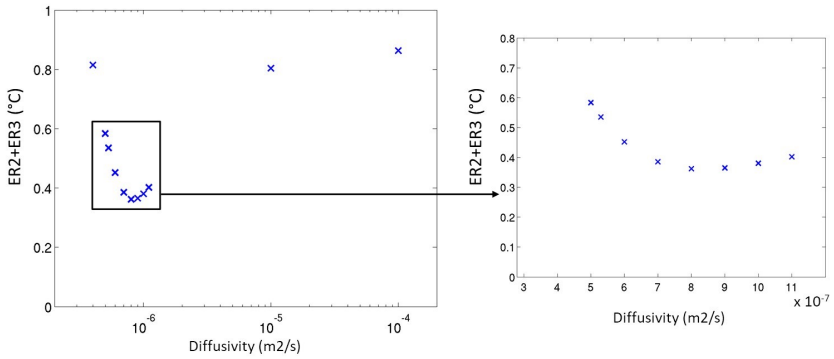

Figure B.15: Difference between simulated and measured temperatures, $(ER2 + ER3)$, as a function of the limestone diffusivity. Left: semi-log scale - Right: zoom on the outlined rectangle, with linear scale.

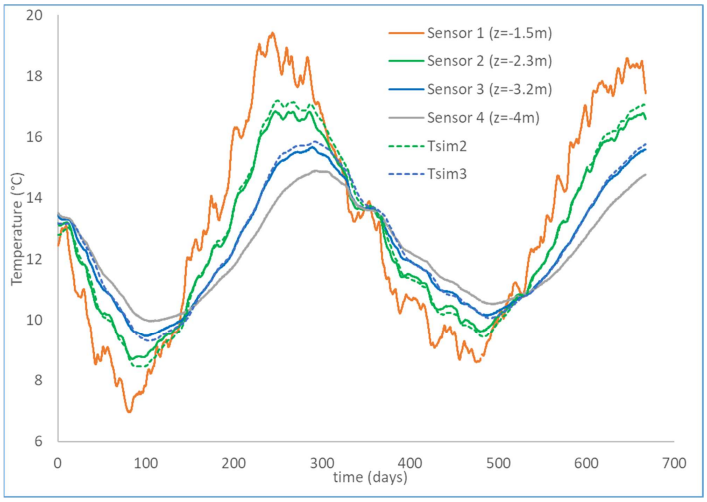

Figure B.16: Comparison between experimental data (continuous lines) and simulated temperatures (dotted lines) for sensors 2 and 3, with $a_r = 8 \times 10^{-7} \mathrm{m}^2.\mathrm{s}^{-1}$. The data corresponding to sensors 1 and 4 are used as boundary conditions of the 1D conductive model.

References

[1] L. Quindos, A. Bonet, N. Diaz-Caneja, P. Fernandez, I. Gutierrez, J. Solana, J. Soto, E. Villar, Study of the environmental variables affecting the natural preservation of the Altamira Cave paintings located at Santillana del Mar, Spain, Atmospheric Environment (1967) 21 (1987) 551 – 560.

[2] S. Sánchez-Moral, V. Soler, J. Cañaveras, E. Sanz-Rubio, R. Van Grieken, K. Gysels, Inorganic deterioration affecting the Altamira Cave, N Spain: quantitative approach to wall-corrosion (solutional etching) processes induced by visitors, Science of The Total Environment 243-244 (1999) 67 – 84.

[3] D. Lacanette, S. Vincent, A. Sarthou, P. Malaurent, J.-P. Caltagirone, An Eulerian/Lagrangian method for the numerical simulation of incompressible convection flows interacting with complex obstacles: Application to the natural convection in the Lascaux cave, Int. J. Heat Mass Transfer (2009) 2528–2542.

[4] P. Malaurent, J. Brunet, D. Lacanette, J.-P. Caltagirone, Contribution of numerical modelling of environmental parameters to the conservation of prehistoric cave paintings: the example of Lascaux cave, Conservation and Management of Archaeological Sites 8 (2007) 59–76.

[5] R. Ginet, Etude écologique de la grotte de la Balme, Isère, Bull. biologique de la France et de la Belgique 85 (1951) 422–447.

[6] D. Culver, T. Pipan, The biology of caves and other subterranean habitats, Oxford University Press, 2009.

[7] D. Sánchez-Fernández, V. Rizzo, A. Cieslak, A. Faille, J. Fresneda, I. Ribera, Thermal niche estimators and the capability of poor dispersal species to cope with climate change, Scientific Reports 6 (2016) 23381.

[8] P.-Y. Jeannin, A. Malard, D. Rickerl, E. Weber, Assessing karst-hydraulic hazards in tunneling–the Brunnmühle spring system–Bernese Jura, Switzerland, Environmental Earth Sciences 74 (2015) 7655–7670.

[9] A. Borsato, V. E. Johnston, S. Frisia, R. Miorandi, F. Corradini, Temperature and altitudinal influence on karst dripwater chemistry: Implications for regional-scale palaeoclimate reconstructions from speleothems, Geochimica et Cosmochimica Acta 177 (2016) 275–297.

[10] R. C. Casteel, J. L. Banner, Temperature-driven seasonal calcite growth and drip water trace element variations in a well-ventilated texas cave: Implications for speleothem paleoclimate studies, Chemical Geology 392 (2015) 43–58.

[11] C. Andrieux, Contribution à l'étude du climat des cavités naturelles des massifs karstiques, Ph.D. thesis, Université de Bordeaux, France, 1969.

[12] F. Bourges, P. Genthon, D. Genty, M. Lorblanchet, E. Mauduit, D. D'Hulst, Conservation of prehistoric caves and stability of their inner climate: Lessons from Chauvet and other French caves, Science of The Total Environment 493 (2014) 79 – 91.

[13] J. Brunet, J. Marsal, P. Vidal, Lascaux : où en sont les travaux de conservation ?, Archéologia 149 (1980).

[14] C. Andrieux, Etude des circulations d'air dans la grotte de Niaux: conséquences, Karstologia 1 (1983) 19–24.

[15] A. Al-Omari, X. Brunetaud, K. Beck, M. Al-Mukhtar, Effect of thermal stress, condensation and freezing-thawing action on the degradation of stones on the Castle of Chambord, France, Environ Earth Sci 71 (2014) 3977–3989.

[16] J.-B. Fourier, Théorie analytique de la chaleur, Gauthier-Villars, 1822.

[17] D. Domínguez-Villar, I. J. Fairchild, A. Baker, R. M. Carrasco, J. Pedraza, Reconstruction of cave air temperature based on surface atmosphere temperature and vegetation changes: Implications for speleothem palaeoclimate records, Earth and Planetary Science Letters 369-370 (2013) 158 – 168.

[18] D. Domínguez-Villar, S. Lojen, K. Krklec, A. Baker, I. J. Fairchild, Is global warming affecting cave temperatures? experimental and model data from a paradigmatic case study, Climate dynamics 45 (2015) 569–581.

[19] H. S. Carslaw, J. C. Jaeger, Conduction of Heat in Solids, Oxford Clarendon Press, 1959.

[20] H. Schoeller, La température des eaux souterraines, Laboratoire de Géologie de la Faculté des Sciences, Bordeaux, France, 1949.

[21] C. R. De Freitas, R. N. Littlejohn, Cave climate: Assessment of heat and moisture exchange, Journal of Climatology 7 (1987) 553–569.

[22] C. De Freitas, A. Schmekal, Condensation as a microclimate process: measurement, numerical simulation and prediction in the Glowworm Cave, New Zealand, International Journal of Climatology 23 (2003) 557–575.

[23] C. De Freitas, S. Antje Anna, Studies of condensation/evaporation processes in the Glowworm Cave, New Zealand, International Journal of Speleology 35 (2006).

[24] P. Malaurent, D. Lacanette, J. Brunet, J. Riss, Climatologie du milieu souterrain à lascaux: d'une étude globale à la microclimatologie des parois, Documents d'archéologie française 105 (2011) 121–142.

[25] L. Laiz, J. Gonzalez, C. Saiz-Jimenez, Microbial communities in caves: ecology, physiology, and effects on paleolithic paintings, Art, biology, and conservation: Biodeterioration of works of art (2003) 210–225.

[26] National Research Council, Basic Research Opportunities in Earth Science, The National Academies Press, Washington, DC, 2001.

[27] G. Badino, Underground drainage systems and geothermal flux, Acta carsologica 34 (2005).

[28] B. Lismonde, Climatologie du monde souterrain., Édition du Comité Départemental de Spéléologie de l'Isère, Grenoble., 2002.

[29] M. Luetscher, P. Jeannin, Temperature distribution in karst systems: the role of air and water fluxes, Terra Nova 16 (2004) 344–350.

[30] H. Schoeller, Étude géologique, hydrogéologique et climatologique de la grotte de lascaux pendant le cycle 1964–1965, Rapport pour la première commission scientifique internationale de la grotte de Lascaux, Université Bordeaux1, France, 97p (1965).

[31] J. Vouvé, J. Brunet, P. V. et, J. Marsal, Les oeuvres rupestres de Lascaux (Montignac, France): maintien des conditions de conservation, Studies in Conservation 28 (1983) 107–116.

[32] E. Cussler, Diffusion mass transfer in fluid systems, Cambridge University Press, 1997.

[33] A. Adamson, Physical Chemistry of Surfaces, J. Wiley, 1990.

[34] F. P. Incropera, D. D. Dewitt, T. D. Bergman, A. S. Lavine, Fundamentals of Heat and Mass Transfer, Wiley international edition, New York, 2007.

[35] E. Sparrow, R. Cess, Radiation Heat Transfer, McGraw–Hill Book Company, 1978.

[36] A. Bejan, Convection heat transfer, John Wiley and sons, 1995.

[37] J. Riddick, W. Bunger, T. Sakano, Organic Solvents: Physical Properties and Methods of Purification, John Wiley and sons, 1986.

[38] R. W. Hyland, A. Wexter, Formulations for the thermodynamic properties of the saturated phases of H_2O from 173.15 K to 473.15 K, ASHRAE transactions 89 (1983) 500–519.

[39] W. Rohsenow, J. Hartnett, Y. Cho, Handbook of Heat Transfer, McGraw-Hill, 1998.

[40] J. Smerdon, M. Stieglitz, Simulating heat transport of harmonic temperature signals in the Earth's shallow subsurface: Lower-boundary sensitivities, Geophysical Research Letters 33 (2006).

[41] N. Houillon, R. Lastennet, A. Denis, P. Malaurent, M. S., N. Peyraube, Assessing cave internal aerology in understanding carbon dioxide (CO2) dynamics: implications on calcite mass variation on the wall of Lascaux Cave (France), Environmental Earth Sciences 76:170 (2017).

[42] R. Buecher, Pre-development studies at Kartchner Caverns, in: National Cave Management Symposium Proceedings, Bowling Green, Kentucky.

[43] N. Houillon, Inorganic carbon dynamics into the soil-epikarst-cavity continuum of the Lascaux Cave (Dordogne, France), PhD Thesis, Université de Bordeaux, 2016.

[44] H. Beltrami, L. Kellman, An examination of short- and long-term air-ground temperature coupling, Global and Planetary Change 38 (2003).

[45] Y. Li, D. Ogura, S. Hokoi, I. Takeshi, Effects of emergency preservation measures following excavation of mural paintings in Takamatsuzuka Tumulus, Journal of Building Physics 36 (2012).

[46] Y. Li, D. Ogura, S. Hokoi, J. Wang, I. Takeshi, Predicting hygrothermal behaviors of the underground stone chamber with 3-D modeling for restraining water-related damages on mural paintings, Journal of Asian Architecture and Building Engineering 13 (2014).